

Development and Characterization of $\text{Ba}_{0.5}\text{Sr}_{0.5}(\text{Co}_{1-x}\text{Mg}_x)_{0.2}\text{Fe}_{0.8}\text{O}_3$ Cathode Materials System for Low-Temperature Solid Oxide Fuel Cell (LT-SOFC) Applications

P. V. C. K. Subhashini¹ · K. V. D. Rajesh²

Received: 23 March 2022 / Accepted: 11 July 2022 / Published online: 20 August 2022
© The Indian Institute of Metals - IIM 2022

Abstract Cathode powders of $\text{Ba}_{0.5}\text{Sr}_{0.5}(\text{Co}_{1-x}\text{Mg}_x)_{0.2}\text{Fe}_{0.8}\text{O}_3$ system (where $x=0, 0.2, 0.4, 0.6, 0.8, 1$) were prepared by solid-state reaction route with an objective to reduce the coefficient of thermal expansion (CTE) by lowering Co concentration and by doping Mg for low-temperature solid oxide fuel cell (SOFC) applications. The relative density of the produced cathodes was measured, and from the values, the presence of porosity was observed. With the increased sintering temperature from 900 to 1175 °C, the density was significantly increased. X-ray diffraction analysis was carried out for all the samples, and formation of no new phases was observed. The average crystallite size was measured as ~ 18 nm with perovskite type structure. The lattice parameters were calculated, and the unit cell dimension (a) was measured as increased with the increased content of Mg. The temperature-dependent electric conductivity of the prepared samples was measured from room temperature to 800 °C. Highest conductivity was observed for the cathode with $\text{Co}_{0.08}$ and $\text{Mg}_{0.12}$ composition. The presence of Co showed profound effect on increasing the electric conductivity of the cathode material compared with Mg. However, coefficient of thermal expansion (CTE) was observed as lower ($13.5 \times 10^{-6}/^\circ\text{C}$) for Mg-rich and Co-free cathode, which is favourable for SOFC applications. The results demonstrate

the promising role of doping Mg ion in developing low-temperature SOFCs.

Keywords Solid oxide fuel cell · Mg doping · Electric conductivity · Coefficient of thermal expansion · Porosity

1 Introduction

The quest for alternate strategies for the generation of clean power to address the issues associated with fossil based fuels in power generation led to the development of several renewable energy systems including power generation from wind, solar and geothermal routes, etc. On the other hand, being electrochemical devices, fuel cells convert chemical energy directly to electrical energy efficiently with negligible emissions and noise [1]. Power generation from alkaline fuel cells (AFCs), polymer electrolyte membrane fuel cells (PEMFCs), molten carbonate fuel cells (MCFCs), phosphoric acid fuel cells (PAFCs) and solid oxide fuel cells (SOFCs) are the potential developments in the fuel cell technology [2–6]. Among them, SOFCs are promising in the context of operating temperatures, choice of fuel selection, low-cost electrode materials, and clean operation to convert chemical energy to electrical energy. Several fuels such as hydrocarbons, biomass, coal gas, natural gas can be directly used in SOFCs [7]. To reduce the operational complexity at high temperatures, interest in developing low-temperature (< 800 °C) SOFCs is growing [8]. However, with the decreased operational temperatures, electrolyte conductivity and electrode activities are significantly decreased, which affect the performance of the fuel cell [9, 10]. At lower temperatures, electrode polarization losses are higher at the interface of the electrolyte and cathode. This issue can be addressed by two strategies. The first strategy involves

✉ P. V. C. K. Subhashini
subha.pvck@gmail.com

K. V. D. Rajesh
kanchurajesh@kluniversity.in

¹ Research Scholar, Department of Mechanical Engineering, Koneru Lakshmaiah Education Foundation, Vaddeswaram, Vijayawada, Andhra Pradesh 522502, India

² Department of Mechanical Engineering, Koneru Lakshmaiah Education Foundation, Vaddeswaram, Vijayawada, Andhra Pradesh 522502, India

altering the composition of the cathode to achieve better diffusion and oxygen exchange kinetics by keeping control on coefficient of thermal expansion (CTE). The second strategy focuses on microstructure optimization at the interface of the electrolyte and cathode to increase the length of triple-phase boundaries (TPBs) [11].

Developing new materials for cathodes has become one of the prime research areas in producing high-performance low-temperature SOFCs. Perovskite structured (ABO_3) systems containing A and B-cations are potential materials for cathodes. $NdBa_{1-x}Co_2O_{5+\delta}$ ($x=0.00-0.06$) [12], $LnBa_{0.5}Sr_{0.5}Co_{2-x}Fe_xO_{5+\delta}$ ($x=0, 0.25, 0.5, 0.75$ and 1.0) [13], $Sm_{0.5}Sr_{0.5}CoO_3$ [14], $Ba_{0.5}Sr_{0.5}Co_{0.8}Fe_{0.2}O_{3-\delta}$ (BSCF) and $(La_{0.6}Sr_{0.4})_{0.9}Co_{0.8}Fe_{0.2}O_{3-\delta}$ [15], $SrCo_{0.9}Nb_{0.1}O_{3-\delta}$ [16], $Ca_2Fe_2O-Ce_{0.9}Gd_{0.1}O_{1.95}$ [17] and $BaCo_{0.4}Fe_{0.4}Zr_{0.1}Y_{0.1}O_{3-\delta}$ [18] are the most widely investigated materials for SOFCs applications. In addition to the chemical composition, microstructure of the materials also significantly influences the performance of the SOFCs. Nanostructured materials offer several advantages in wide range of applications due to their high volume to surface area. In developing SOFCs, using nanostructured electrolyte and cathode materials significantly enhances the performance of the cell [19, 20]. Among the aforementioned material systems, BSCF is promising for low-temperature SOFC applications [21, 22]. However, the presence of higher Co content in BSCF leads to higher CTE. Compared with basic BSCF structure, ion-doped BSCFs have demonstrated higher performance as reported in the recent literature. For example, Liu et al. [23] demonstrated the positive role of doping La, Ce, and Pr at B-site of BSCF cathodes on increasing the oxygen reduction activity. Zeng et al. [24] also produced Zn-doped BSCF cathode material that exhibited higher electrocatalytic activity for the oxygen reduction reaction. It can be learnt from the literature that several reported works demonstrated potential of doping Nb^{3+} , Mo^{6+} and Y^{3+} into BSCF to enhance the performance of the cell [25–27]. Information on doping Mg ion into BSCF and evaluating its efficacy as cathode material is insufficient in the literature. Therefore, in the current research work, BSCF system with lower Co by doping Mg has been prepared in order to reduce CTE. The produced BSCF-based cathode and cerium-based electrolyte powders were prepared and characterized. The electrical conductivity and CTE properties of the cathode materials were investigated.

2 Experimental Details

High-purity (99%) oxide and carbonate powders of the metal cations $BaCO_3$ (Merck Ltd), $SrCO_3$ (Merck Ltd), Co_3O_4 (Sigma-Aldrich), Fe_2O_3 (Sigma-Aldrich) and MgO (Sigma-Aldrich) were used as raw

materials for the preparation of cathode powders of $Ba_{0.5}Sr_{0.5}(Co_{1-x}Mg_x)_{0.2}Fe_{0.8}O_3$ system (where $x=0, 0.2, 0.4, 0.6, 0.8, 1$). Different compositions were prepared by mixing appropriate amounts of oxides and carbonates in wt.%. For the sake of convenience, the compositions are abbreviated as: $x=0$ with BSCF, $x=0.2$ with BSCMF2, $x=0.4$ with BSCMF4, $x=0.6$ with BSCMF6, $x=0.8$ with BSCMF8 and $x=1$ with BSMF.

Ball milling was carried out using zirconia balls as the milling medium. Powder-to-ball weight ratio was maintained as 1:2 for all the compositions. Initially, the powders were mixed with a solvent (isopropyl alcohol) and then the slurries were ball milled for 24 h to achieve homogeneous mixing of the cathode powders. All the ball milled cathode powders were calcined at $900\text{ }^\circ\text{C}$ for 2 h in a high-temperature box furnace for the phase formation of the powders. The calcined powders were then ground for 30 min to break the calcined lumps using a mortar and pestle. Then, the powders were sieved to filter coarse particles and then mixed with 2 wt.% binder (methyl cellulose). Then, the powders were ball milled for 6 h by using zirconia as the grinding media with powder-to-ball weight ratio of 1:2 in an organic solvent (isopropyl alcohol). After ball milling, the powder was collected and dried at $80\text{ }^\circ\text{C}$. Then, the powders were sieved to get granules of the powder to be compacted.

The powders were then compacted as pellets of size 10 mm diameter \times 2 mm thickness by uniaxially compressing using a hydraulic press in a stainless steel die of 10 mm diameter under a load of 4 tons. The amount of cathode powder used for the compaction was 0.5 g for each composition of $Ba_{0.5}Sr_{0.5}(Co_{1-x}Mg_x)_{0.2}Fe_{0.8}O_3$ system. The green pellets were then sintered to produce solid compacts. Initially, a heating rate of $2\text{ }^\circ\text{C}/\text{min}$ was adopted up to $550\text{ }^\circ\text{C}$ for 30 min to evaporate the binder. Then, the heating rate was altered to $2.5\text{ }^\circ\text{C}/\text{min}$ up to $1175\text{ }^\circ\text{C}$ with 4 h of soaking time. The green compacts of gadolinium-doped cerium (GDC) electrolyte having 10 mm diameter and 3 mm thickness were prepared by the similar procedure. Then, the GDC green compacts were sintered at a temperature of $1500\text{ }^\circ\text{C}$ with 2 h of soaking time. Figure 1 shows the sintering cycle adopted to produce GDC compacts.

The density of the sintered pellets was measured by Archimedes principle using water as the medium. Bulk density of the sintered samples was measured by using Sartorius balance with density measuring kit (Sartorius, AG37070 Goettingen, Germany). Initially, the dry weight (D) of the sample was measured, followed by boiling the same sample in distilled water for about 40 min and allowing to cool down to the room temperature. Then, the saturated weight (W) and the suspended weight in water (S) were measured accurately. The bulk density of the sample was calculated by using Eq. (1).

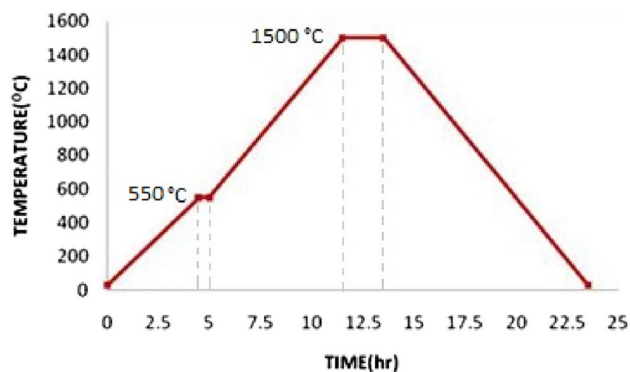


Fig. 1 Sintering cycle adopted to produce GDC compacts

$$\text{Bulk density} = D/W - S \quad (1)$$

Theoretical density of the samples was also calculated by using Eq. (2) [28].

$$\rho = nM/Na^3 \quad (2)$$

where n is the number of formula units in a cell, M is the molecular weight of the composition, N is the Avogadro number, and ‘ a ’ is the lattice constant.

An attempt was made to achieve a maximum density in the cathode material by changing the heating rate from 2.5 to 10 °C/min by using a dilatometer (which can be used for sintering and densification studies). The BSCF sample was sintered in the dilatometer at 1175 °C for 1 h at a heating rate of 10 °C/min. The synthesized cathode materials were characterized by X-ray diffraction (XRD) analysis. The diffraction patterns were recorded from 5° to 90° with an analytical system (Bruker’s AXS Model No: D8 Advance System, Germany) using Cu K α ($\lambda = 1.542\text{\AA}$) radiation with an accelerating voltage of 40 kV. Data were collected with a counting rate of 3°/min. The crystallite size was calculated by the Debye–Scherrer’s formula as given in Eq. (3):

$$S = 0.9\lambda/\beta \cos\theta \quad (3)$$

where S is the crystallite size, λ is the wavelength of X-rays, β is the full width half maxima in radians, and θ is the angle in degrees at which the intensity peak appears.

Scanning electron microscope (SEM) images of the samples were obtained for microstructure analysis. DC four-probe method was adopted for electrical conductivity measurement, and dilatometry was also carried out to measure coefficient of thermal expansion of the samples.

Table 1 Bulk, theoretical and relative densities of BSCMF System of samples

Sample	Bulk density (g/cc) 1175 °C/4 h	Theoretical density (g/ cc)	Relative density (g/cc) 1175 °C/4 h
BSCF	4.90	5.84	83%
BSCMF2	5.21	5.85	89%
BSCMF4	5.12	5.85	87%
BSCMF6	5.17	5.82	88%
BSCMF8	5.23	5.78	90%
BSMF	5.27	5.79	91%

3 Results and Discussion

The bulk densities of the samples obtained from the Archimedes principle and theoretical densities calculated from Eq. (3) are listed in Table 1. Relative densities of the samples with respect to theoretical densities are also calculated and are presented in Table 1. From the data, it can be observed that the densities obtained for BSCMF samples sintered at 900 and 1175 °C are in the range of 80–90%. It is true that the solid compacts produced from powder metallurgy route exhibit certain porosity. The evaporated binder leaves considerable volume of cavity between the compacted particles. The densification process involves initial neck formation at the contact regions of the particles during heating. Then, the neck growth and grain growth happens by reducing the cavity volume. The increased grain boundary results in discontinuous pores and further leads to densification of the compact [29]. However, the presence of porosity is inevitable in the sintered compacts. In the present work, the sintered cathode materials exhibit considerable amount of porosity. Interestingly, Co free BSMF has shown a significant reduction in the porosity as reflected in the increased relative density after sintering at 1175 °C compared with all the other compositions. The atomic radius of doped ions influences the lattice volume expansion or contraction [30, 31]. Doping increase in the volume due to an increase in the lattice constant with increased concentration of Mg at cobalt site in BSCF resulting in increased relative density of the system of compositions [28].

XRD patterns of cathode powders of BSCMF system calcined at 900 °C for 2 h are shown in Fig. 2. The as-synthesized powders show well-crystallized cubic perovskite oxide structure, and there are no peaks corresponding to any impurity identified in the XRD patterns. All the peaks in the XRD patterns are indexed corresponding to the cubic perovskite structure with the space group of Pm3m.

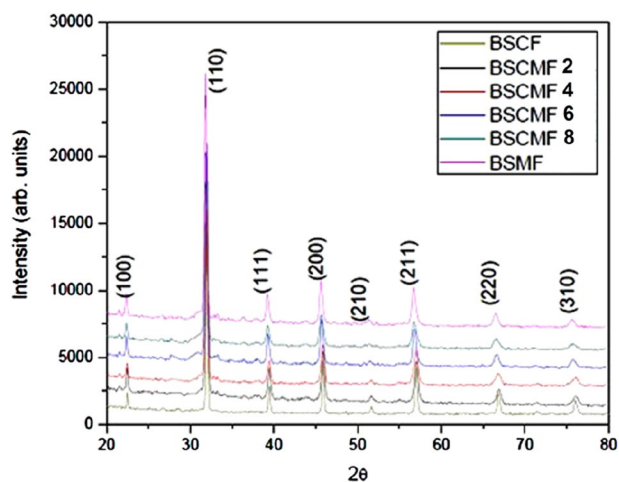


Fig. 2 XRD patterns of the samples

Table 2 Lattice constant values of BSCMF system

Sample	2θ (degree)	$d_{(1,1,0)}$ (Å)	Lattice constant (a)
BSCF	31.97	2.795	3.954 Å
BSCMF2	31.95	2.797	3.956 Å
BSCMF4	31.92	2.800	3.960 Å
BSCMF6	31.84	2.807	3.969 Å
BSCMF8	31.83	2.808	3.971 Å
BSMF	31.79	2.811	3.975 Å

The lattice constants of all the samples have been calculated from the XRD results and are shown in Table 2. With the increased Mg content, the lattice parameters calculated for cathode powders are also varied from 3.954 to 3.975 Å due to the lattice expansion. From the XRD patterns, a marginal peak shift (110) towards lower 2θ values with the increased content of Mg is observed which also confirms the increased lattice volume. The average crystallite size of these powders was calculated by Scherrer equation as ~ 18 nm. While preparing the polycrystalline materials by sintering, with the increased sintering temperature, usually, crystallite size is grown. Lower sintering temperature reduces the densification of the green compact. Hence, selecting the appropriate sintering temperature is crucial in developing components through sintering. Hence, in the present work, sintering temperature has been selected as 1175 °C.

Table 3 Tolerance Factor values of BSCMF system

Tolerance factor	BSCF	BSCMF2	BSCMF4	BSCMF6	BSCMF8	BSMF
S' ($\text{Co}^{+4}, \text{Fe}^{+4}, \text{Mg}^{+2}$)	1.047	1.0432	1.0389	1.0346	1.0302	1.025
S'' ($\text{Co}^{+3}, \text{Fe}^{+3}, \text{Mg}^{+2}$)	1.014	1.0122	1.0097	1.0071	1.0046	1.002
S''' ($\text{Co}^{+2}, \text{Fe}^{+3}, \text{Mg}^{+2}$)	1.0015	1.0016	1.0017	1.0018	1.0019	1.002

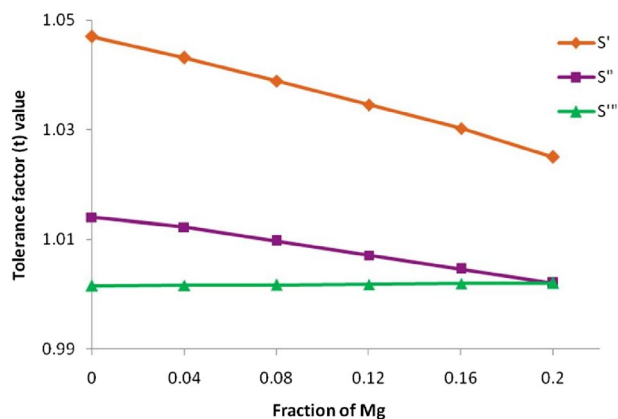


Fig. 3 Tolerance factor values obtained from XRD analysis

The structural stability of perovskite-type compound is usually determined by the tolerance factor as described in Eq. (4):

$$t = (r_A + r_O) / 2^{1/2} (r_B + r_O) \quad (4)$$

where 't' denotes the tolerance factor, and r_O , r_A , r_B are the effective ionic radius of oxygen ion, A-site ion, and B-site ion, respectively. When t is around 1, the compounds are in steady cubic perovskite-type and exhibit excellent property. For BSCMF system, except for Mg, the valence of B-site ion (Co/Fe) is changeable; thus, the tolerance factor should be calculated in three situations: (i) The Co/Fe are in quadri-valence (S'), (ii) the Co/Fe are in tri-valence (S''), (iii) the Co/Fe are in both the tri-valence and bivalence (S'''). The calculated tolerance factor values are given in Table 3 and compared in Fig. 3.

As shown in Fig. 3, with increased Mg content, the tolerance factor has been reduced and approached 1. This observation confirms that the Mg substitution enhances the structure stability in the cathode material. The data of ionic radii were taken from Shannon radii for respective coordination numbers.

Figure 4 shows the typical SEM images of BSMF and BSCF sintered at 1175 °C. From the images, significant porosity can be observed in the sintered samples. Compared with the sintered sample, cathode material produced by using dilatometer exhibits lower porosity with 99% density (Fig. 5). Higher densities can be achieved by varying the sintering conditions such as sintering temperature, time, heating and cooling rate, and the sintering atmosphere (O_2 , N_2 , vacuum). With the higher heating rate

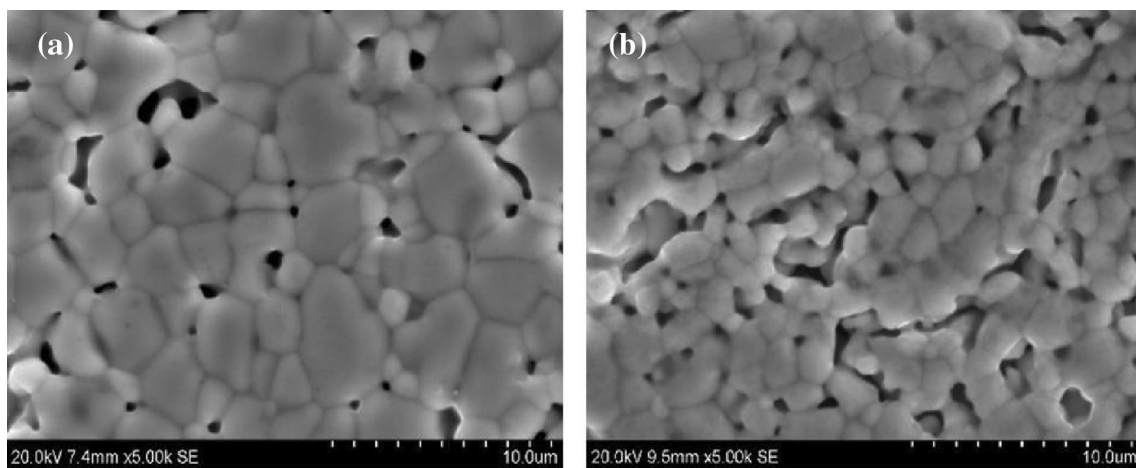


Fig. 4 Typical SEM images showing sintered microstructure of the cathodes: **a** BSMF sintered at 1175 °C/4 h and **b** BSCF sintered at 1175 °C/4 h

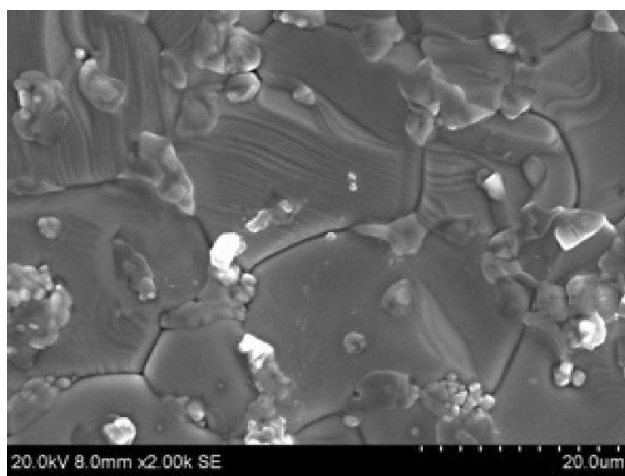


Fig. 5 SEM image showing microstructure of BSCF cathode sample

adopted by using dilatometer, maximum density has been achieved.

For perovskite mixed ionic-electronic conductors (MIECs), the co-presence of electronic holes and oxygen vacancies makes them simultaneously exhibit both electronic and ionic conductivity [32]. As electronic conductivity is at least one order higher than the ionic conductivity, the measured values (total conductivity) can be mainly referred to electronic conductivity. Figure 6 shows the temperature dependence of electrical conductivity of dense BSCMF pellets in air measured from room temperature to 800 °C.

It can be observed from Fig. 6 that the conductivity has been increased (p-type semi-conductivity) and reaches a maximum value between 300 and 400 °C and then decreases (pseudo-metallic behaviour) with further heating. The decrease in the conductivity is mainly associated with the

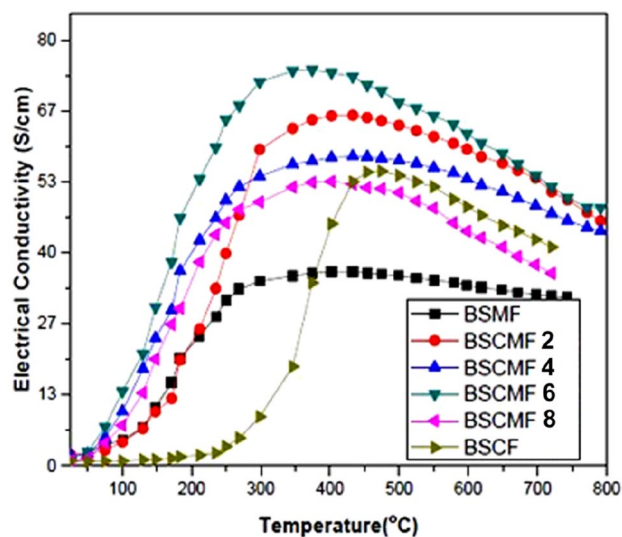


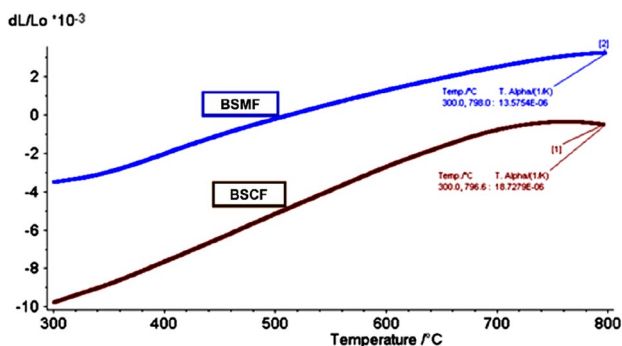
Fig. 6 Electric conductivity of BSCMF samples at different temperatures

loss of the lattice oxygen due to the reduction of the B-site ions (cobalt and iron) at elevated temperature [15]. The peak electrical conductivity values of BSCMF pellets are given in Table 4.

The electrical conductivity values of BSCMF samples are in the range of 50–75 S/cm except for BSMF (35 S/cm). Doping Co has immense effect in enhancing the electric conductivity of the cathode material compared to Mg. With the presence of Co, the electric conductivity is higher in cathode materials. The lower conductivity in BSMF is due to the fact that Mg holds fixed bivalent state by which it decreases the total concentration of B-sites that participate in the electronic transport processes, and

Table 4 Electrical conductivity values of BSCMF system

Sample	Electrical conductivity (σ), (S/cm)
BSCF	56
BSCMF2	54
BSCMF4	60
BSCMF6	74
BSCMF8	66
BSMF	35

**Fig. 7** Comparison of coefficient of thermal expansion (CTE) of BSCF and BSMF samples

hence does not contribute to the conductivity. Highest conductivity is observed for the composition with $\text{Co}_{0.08}$ and $\text{Mg}_{0.12}$. From the overall observations, the conductivities of BSCMF samples are relatively lower, but this does not significantly affect the cathode performance since compared with the electronic conductivity (total conductivity), the ionic conduction related to large oxygen vacancy concentration is more important for an SOFC cathode.

Thermal expansion measurement (CTE) of the cathode material with two end compositions BSCF and BSMF is evaluated. Figure 7 shows the significant decrease in coefficient of thermal expansion value with Mg addition at the cobalt site of BSCF composition. The value of CTE for BSCF has been measured as $18.7 \times 10^{-6}/^\circ\text{C}$ and for BSMF as $13.5 \times 10^{-6}/^\circ\text{C}$. The CTE value of BSMF composition is very near to the CTE of GDC $12 \times 10^{-6}/^\circ\text{C}$. From the results, it can be understood that the BSMF formulation can be a viable cathode material to be used with GDC electrolyte for low-temperature SOFC operation [33, 34]. It is also understood that the addition of Co helps to produce cathode materials with higher electrical conduction.

4 Conclusions

In the present work, powder metallurgy route has been adopted to synthesize cathodes of $\text{Ba}_{0.5}\text{Sr}_{0.5}(\text{Co}_{1-x}\text{Mg}_x)_{0.2}\text{Fe}_{0.8}\text{O}_3$ system (where $x=0, 0.2, 0.4, 0.6, 0.8, 1$) for low-temperature solid oxide fuel cell (SOFC) applications. From the density measurements, higher porosity was measured for the compacts sintered at 900°C . With the increased sintering temperature (1175°C), relative density of the compacts was measured as increased up to 91%. X-ray diffraction (XRD) studies indicating perovskite-type structure of the produced cathodes with no trace of any impurities. The average crystallite size was measured as ~ 18 nm for the prepared powders. The increased Mg doping in the system has increased the unit cell dimension. From the electric conductivity measurement done at different temperatures, higher value was recorded for the cathode with $\text{Co}_{0.08}$ and $\text{Mg}_{0.12}$ composition. Doping of Co showed profound effect to increase the electrical conductivity of the cathode material compared with Mg. Coefficient of thermal expansion (CTE) measurements for both the end compositions showed lower value ($13.5 \times 10^{-6}/^\circ\text{C}$) for Mg-rich cathode. Hence, from the results, it can be concluded that BSFO cathode system doped with Co and Mg can be successfully produced by powder metallurgy which exhibit increased electric conductivity. The presence of Mg decreases the CTE, which is an essential requirement for the cathode material in developing low-temperature SOFCs.

References

1. Saddam H, Li Y, *Energy Transitions*, 2021, <https://doi.org/https://doi.org/10.1007/s41825-020-00029-8>.
2. Mclean G F, NietT, Prince-Richard S, DjilaliN, *Int. J. Hydrogen Energy* **27** (2002) 507.
3. SammesN, BoveR, Stahl K, *Curr Opin Solid State Mater Sci* **8** (2004) 372.
4. Zhang H, Shen P K, *Chem Soc Rev* **41** (2012) 2382.
5. Dicks A L, *Curr Opin Solid State Mater Sci* **8** (2004) 379.
6. Brett D J, Atkinson A, Brandon N P, Skinner S J, *Chem Soc Rev* **37** (2008) 1568.
7. SinghalS C, Kendal K, *High Temperature Solid Oxide Fuel Cells*, Elsevier, Netherlands (2003)
8. Istomin SY, Antipov E V, *Russ Chem Rev* **82**(2013) 686.
9. Lee K T, WachsmannE D, *MRS Bull* **39** (2014) 783.
10. An J, Shim J H, Kim Y, Park J S, Lee W, Gur T M, PrinzF B, *MRS Bull* **39** (2014) 798.
11. Chen Y, Zhou W, Ding D, Liu M, Ciucci F, Tade M, Shao Z, *Adv Energy Mater* **5** (2015) 1500537
12. Sun J, Liu X, Han F, Zhu L, Bi H, Wang H, Yu S, Pei L, *Solid State Ionics* **288**, (2016) 54.
13. Choi S, Yoo S, Kim J, Park S, Jun A, Sengodan S, Kim J, Shin J, Jeong H Y, Choi Y, Kim G, Liu M, *Sci Rep* **3** (2013) 3.
14. Dai H, Kou H, Tao Z, Liu K, Xue M, Zhang Q, Bi L, *Ceram Int* **46** (2020) 6987.
15. Baumann FS, Fleig J, Cristiani G, Stuhlhofer B, Habermeier H U, Maier J, *J Electrochem Soc* **154**, (2007) B931.

16. Wang B, Bi L, Zhao X S, *Ceram Int* **44** (2018) 5139.
17. Lee SJ, Yong SM, Kim DS, Kim D K, *Int J Hydrogen Energy* **37** (2012) 17217.
18. Duan C, Hook D, Chen Y, Tong J, O'Hayre R, *Energy Environ Sci* **10**(2017) 176.
19. Martinelli H, Lamas D G, Leyva A G, Sacanell J, *Mater Res Express* **5**(2018) 075013.
20. Abdalla A M, Hossain S, Azad AT, Petra PMI, Begum F, Eriksson SG, Azad A K, *Renew Sustain Energy Rev* **82** (2018) 353.
21. Habiballah AS, Nafisah O, Abdul MJ, *Ceram Int* **46(14)** (2020) 23262.
22. Zhao S, Tian N, Yu J, *J Alloys Compd* **825** (2020) 154013.
23. Liu, D, Dou Y, Xia T, Li Q, Sun L, Huo L, Zhao H, *J Power Sources*, **494** (2021) 229778.
24. Zeng Q, Zhang X, Wang W, Zhang D, Jiang Y, Zhou X, Lin B, *Catalysts* **10(2)** (2020) 235.
25. Gou M, Ren R, Sun W, Xu C, Meng X, Wang Z, Qiao J, Sun K, *Ceram Int* **45(12)** (2019) 15696 -15704.
26. Li X, Liu Y, Liu W, Wang C, Xu X, Dai H, Wang X, Bi L, *Sustain Energ Fuels*, **5** (2021) 4261-4267.
27. Meffert M, Unger L S, Störmer H, Sigloch F, Wagner S F, Ivers-Tiffée E, Gerthsen D, *J Am Ceram Soc* **102** (2019) 4929–4942.
28. William D Callister Jr, David G Rethwisch, *Materials Science and Engineering: An Introduction*, 2013, Wiley, USA.
29. Randall G, *Sintering: From Empirical Observations to Scientific Principles*, Elsevier, USA, (2014)
30. Kamila R, Kurniawan B, *IOP Conf Ser: Mater Sci Eng* **496** (2019) 012019.
31. Bilgili O, *Acta Phys Pol A*, **136** (2019) 460-466.
32. Chen G, Feldhoff A, Weidenkaff A et al., *Adv Funct Mater*, **32(6)** (2022) 2105702.
33. Minh-Vien Lea, Dah-Shyang Tsaib, Tuan-Anh Nguyena, *Ceram Int*, **44** (2018) 1726.
34. Tatsumi Ishihara, Nigel M. Sammes, Osamu Yamamoto, *High Temperature Solid Oxide Fuel Cells* **4** (2003) 83.

Publisher's Note Springer Nature remains neutral with regard to jurisdictional claims in published maps and institutional affiliations.

Springer Nature or its licensor holds exclusive rights to this article under a publishing agreement with the author(s) or other rightsholder(s); author self-archiving of the accepted manuscript version of this article is solely governed by the terms of such publishing agreement and applicable law.